PAPER

Magnetohydrodynamics simulation of magnetic flux rope formation in a quadrupolar magnetic field configuration

To cite this article: Sanjay Kumar et al 2023 Plasma Phys. Control. Fusion 65 085008

View the article online for updates and enhancements.

You may also like

- The Role of Magnetic Flux Rope in Ion Acceleration: MHD Simulations and Testparticle Tracing Kun Bai, Yiqun Yu, Huishan Fu et al.
- SPECTROSCOPIC DIAGNOSTICS OF SOLAR MAGNETIC FLUX ROPES USING IRON FORBIDDEN LINE X. Cheng and M. D. Ding
- Evolution of the Nonpotential Magnetic Field in the Solar Active Region 12673 Based on a Nonlinear Force-free Modeling Daiki Yamasaki, Satoshi Inoue, Shin'ichi Nagata et al.

Plasma Phys. Control. Fusion 65 (2023) 085008 (12pp)

https://doi.org/10.1088/1361-6587/acdd1d

Magnetohydrodynamics simulation of magnetic flux rope formation in a quadrupolar magnetic field configuration

Sanjay Kumar^{1,*}, Avijeet Prasad^{2,3}, Sushree S Nayak⁴, Satyam Agarwal^{5,6} and R Bhattacharyya⁵

E-mail: sainisanjay35@gmail.com

Received 9 November 2022, revised 10 May 2023 Accepted for publication 9 June 2023 Published 22 June 2023



Abstract

Magnetic flux ropes (MFRs) play an important role in high-energetic events like solar flares and coronal mass ejections in the solar atmosphere. Importantly, solar observations suggest an association of some flaring events with quadrupolar magnetic configurations. However, the formation and subsequent evolution of MFRs in such magnetic configurations still need to be fully understood. In this paper, we present idealized magnetohydrodynamics (MHD) simulations of MFR formation in a quadrupolar magnetic configuration. A suitable initial magnetic field having a quadrupolar configuration is constructed by modifying a three-dimensional linear force-free magnetic field. The initial magnetic field contains neutral lines, which consist of X-type null points. The simulated dynamics initially demonstrate the oppositely directed magnetic field lines located across the polarity inversion lines (PILs) moving towards each other, resulting in magnetic reconnections. Due to these reconnections, four highly twisted MFRs form over the PILs. With time, the foot points of the MFRs move towards the X-type neutral lines and reconnect, generating complex magnetic structures around the neutral lines, thus making the MFR topology more complex in the quadrupolar configuration than those formed in bipolar loop systems. Further evolution reveals the non-uniform rise of the MFRs. Importantly, the simulations indicate that the pre-existing X-type null points in magnetic configurations can be crucial to the evolution of the MFRs and may lead to the observed brightenings during the onset of some flaring events in the quadrupolar configurations.

1361-6587/23/085008+12\$33.00 Printed in the UK

¹ Department of Physics, Patna University, Patna 80005, India

² Rosseland Centre for Solar Physics, University of Oslo, Postboks 1029 Blindern, 0315 Oslo, Norway

³ Institute of Theoretical Astrophysics, University of Oslo, Postboks 1029 Blindern, 0315 Oslo, Norway

⁴ Center for Space Plasma & Aeronomic Research, The University of Alabama in Huntsville, Huntsville AL 35899, United States of America

⁵ Udaipur Solar Observatory, Physical Research Laboratory, Dewali, Badi Road, Udaipur 313001, India

⁶ Discipline of Physics, Indian Institute of Technology, Gandhinagar 382355, India

^{*} Author to whom any correspondence should be addressed.

Supplementary material for this article is available online

Keywords: magnetohydrodynamics, magnetic reconnections, magnetic flux ropes, EULAG-MHD

(Some figures may appear in colour only in the online journal)

1. Introduction

A magnetic flux rope (MFR) is a bundle of twisted magnetic field lines (MFLs) which wind around a given axis [1]. MFRs play a vital role in the dynamical evolution of diverse plasma systems, such as the laboratory, space, and astrophysical plasmas [2–5]. Particularly, in the solar context, MFRs are believed to be the magnetic structures that can lead to eruptive events in the solar atmosphere, such as solar flares, coronal mass ejections, and prominence eruptions [1, 2]. The twisted field lines of MFRs represent regions of strong currents and facilitate the storage of magnetic energy [1, 6]. These eruptive events release the stored magnetic energy in the form of radiation, mass flow, and accelerated charged particles. Thus, it is crucial to investigate the formation and subsequent evolution of MFRs to gain a comprehensive understanding of solar eruptions.

There are broadly two mechanisms through which an MFR can appear in the solar atmosphere. In the first mechanism, an MFR pre-exists below the solar surface and, due to the magnetic buoyancy, can become unstable and emerge out of the solar surface into the atmosphere [7-10]. In contrast, the second mechanism advocates the formation of MFR in the solar atmosphere itself by magnetic reconnections (MRs) inside sheared magnetic arcades [11–14]. These reconnectionbased studies of MFR formation often rely on the force-free field assumption (i.e. vanishing Lorentz force) of the coronal field. The initiation of MRs and subsequent MFR formation are governed by prescribed (shearing and/or converging) flows at the bottom boundary. Recently, an alternative approach based on non-force-free fields is also developed that supports the non-zero Lorentz force [15-18]. This approach demonstrates the spontaneous onset of MRs in arcades without any prescribed boundary flow, accounting for the development and subsequent evolution of MFRs.

It is noteworthy that the MFR, once formed, can exist as a stable structure and manifest itself in the form of filament/prominence [2]. With time, they can become unstable by ideal magnetohydrodynamics (MHD) instabilities such as the kink instability or the torus instability [19, 20]—leading to eruptions. Alternatively, the MFR can remain in the dynamic phase due to repeated MRs, which further add a significant amount of magnetic fluxes in the MFR—causing a rise and expansion of the MFR [15, 16]. Such rapidly rising MFRs can play a crucial role in the onset of a solar flare and the subsequent evolution of the eruptions [6, 16, 18]. The numerical studies on MFR formation through MRs so far have been predominantly carried out for the bipolar flux

systems [11, 13–15, 18], while far more complex topologies are observed in the extreme-ultraviolet (EUV) observations of the solar corona. Particularly, some observational studies have revealed flaring regions to be associated with quadrupolar magnetic configurations [21–25]. Although quadrupolar configurations have been employed in previous works [26, 27] to assess the magnetic topology and energy storage in the coronal field, not many studies have been conducted to explore the formation and evolution of MFRs in such configurations. Using a flux emergence-based model, [10] has shown the formation of the complex quadrupolar magnetic structures in the solar corona, whereas [28] used a magnetofrictional model for automated detection of MFRs and studying MFR formation in the solar corona. Another recent study by [29] examined the evolution of MFRs in quadrupolar configuration and the role of MFR evolution in solar flares utilizing pre-existing twisted magnetic structures emerging from below the photosphere.

In this work, we explore MFR evolution in terms of their formation from quadrupolar magnetic loops and continuous ascent, mediated via MRs. We simulate the viscous relaxation of an incompressible, thermally inactive, and infinitely conducting plasma from an initial non-equilibrium state to ensure the spontaneous onset of MRs in the MHD simulation [15, 30]. The spontaneity of MRs stems from Parker's magnetostatic theorem [31, 32], according to which a plasma with infinite electrical conductivity and complex magnetic topology cannot achieve an equilibrium state with a continuous magnetic field. The viscous relaxation is in harmony with the magnetostatic theorem—leading to the natural generation of MRs [15, 30]. The initial non-equilibrium state for the relaxation is achieved through the initial non-force-free field, which provides the Lorentz force that initiates dynamics without needing a prescribed flow. Relevantly, a recent study by [33] has suggested the similarity in the MHD of a coronal transient initiated with force-free and non-force-free extrapolated magnetic fields. Furthermore, in the context of the relaxation theory, the minimum-dissipation-rate (MDR) principle results in nonforce-free fields as a relaxed state for externally driven systems [34, 35]. This makes the solar corona, which is driven by the photospheric boundary flows, a suitable candidate for the application of the MDR principle [34]. The physical scales can become under-resolved during the relaxation constrained by the flux-freezing condition. Our numerical scheme intermittently and adaptively regularizes these under-resolved scales by mimicking MRs. The simulated evolution documents the onset of MRs, which lead to the formation of the MFRs in the quadrupolar magnetic configuration. The MFRs are found to

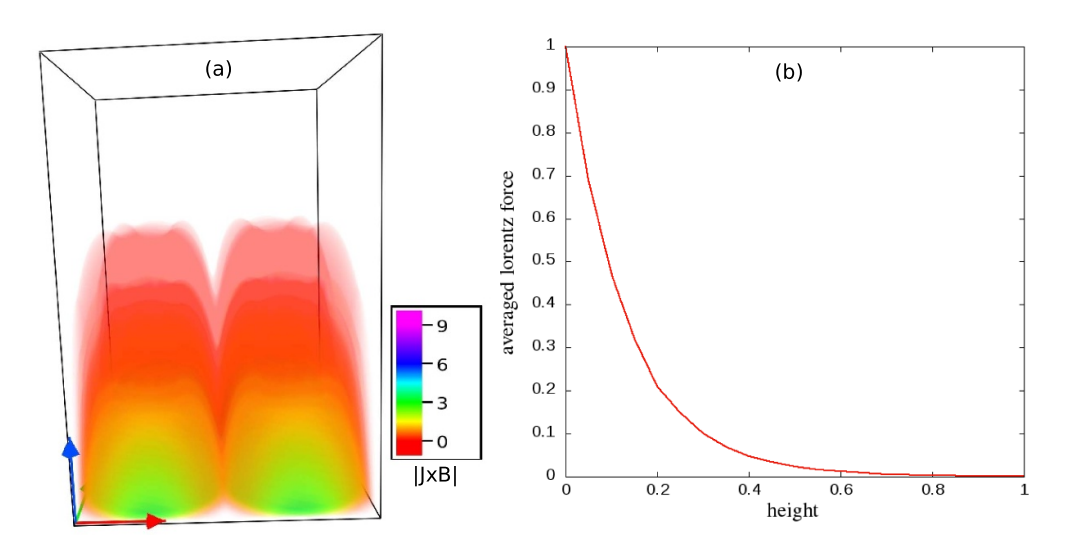


Figure 1. Panel (a) illustrates the distribution of the magnitude of the initial Lorentz force density in the computational domain. Panel (b) plots the magnitude variation of the horizontally averaged Lorentz force density with height. The force density and height are normalized to their maximum values, as our focus is on its decay rate with height. Both panels clearly illustrate the exponential decrease of the force density with height.

be morphologically more complex than the ones generated in the bipolar magnetic loops. Subsequently, the reconnections continue in time and add more magnetic flux to the MFRs, causing the rise of the MFRs.

The paper is organized as follows. The initial magnetic field is described in section 2. The governing MHD equations and the numerical model are discussed in section 3. The simulation results are presented in section 4. Section 5 summarizes these results and discusses the key findings.

2. Initial magnetic field

To achieve a suitable initial magnetic field with quadrupolar configuration, we revise the general construction procedure utilized by [15], which was aimed to study the MFR formation in the bipolar magnetic loops. The Cartesian components of the chosen initial magnetic field **B** are

$$B_x = 0.5 \left[\alpha_0 \sin(x) \cos(y) \exp\left(-\frac{k_0 z}{s_0}\right) - k_0 \cos(x) \sin(y) \exp\left(-\frac{k_0 z}{s_0}\right) \right], \tag{1}$$

$$B_{y} = -0.5 \left[\alpha_{0} \cos(x) \sin(y) \exp\left(-\frac{k_{0}z}{s_{0}}\right) + k_{0} \sin(x) \cos(y) \exp\left(-\frac{k_{0}z}{s_{0}}\right) \right], \tag{2}$$

$$B_z = s_0 \sin(x) \sin(y) \exp\left(-\frac{k_0 z}{s_0}\right),\tag{3}$$

where α_0 , k_0 and s_0 are constants. The constant α_0 and k_0 are related as $k_0 = \sqrt{2 - \alpha_0^2}$. The field **B** is specified in the positive half-space $(z \ge 0)$ of a Cartesian domain Γ , which is

periodic along the lateral directions (ranging from 0 to 2π in x and y) and open along the vertical direction (ranging from 0 to 6π in z). The initial magnetic field **B** supports the nonzero Lorentz force for $s_0 \neq 1$, which contributes to the viscous relaxation. For the simulations, we set $s_0 = 6$ to have an optimal Lorentz force for generating efficient dynamics with a minimal computational cost. Noticeably, for $s_0 = 1$, **B** satisfies the linear force-free equation $\nabla \times \mathbf{B} = \alpha_0 \mathbf{B}$, where α_0 represents the magnetic circulation per unit flux, and is related to the twist of the corresponding MFLs [30]. We set $\alpha_0 = 0.1$ to have sufficiently twisted initial MFLs and, hence, complex magnetic topology (as demanded by the magnetostatic theorem). Moreover, the chosen α_0 corresponds to a high value of k_0 that leads to a steeper exponential decay of the initial Lorentz force (see figure 1). Relevantly, the solar corona is considered to be in the force-free equilibrium state under the low plasma- β approximation [1]. On the other hand, the photosphere with plasma- $\beta \sim 1$ is expected to be non-force-free due to the convective driving [36].

In figure 1(a), we have shown the direct volume renderings of the Lorentz force density, which shows the decay of the Lorentz force with height. In this and the subsequent figures, the arrows in the colors red, green, and blue represent the directions x, y, and z, respectively. To confirm this further, we plot the horizontally averaged Lorentz force density variation with height in figure 1(b). The averaged Lorentz force density falls off sharply with height, such that the upper half of the domain is nearly in a force-free state.

Figure 2 shows the initial magnetic field configuration. In the figure, the lower boundary is superimposed with the B_z values. The multiple polarities in the initial field are shown in figure 2(b), where P1 and P2 mark the positive polarities, while N1 and N2 denote the negative polarities. The polarity inversion lines (PILs) corresponding to the different opposite polarities (P1, N1), (P1, N2), (P2, N1), and (P2, N2) are shown

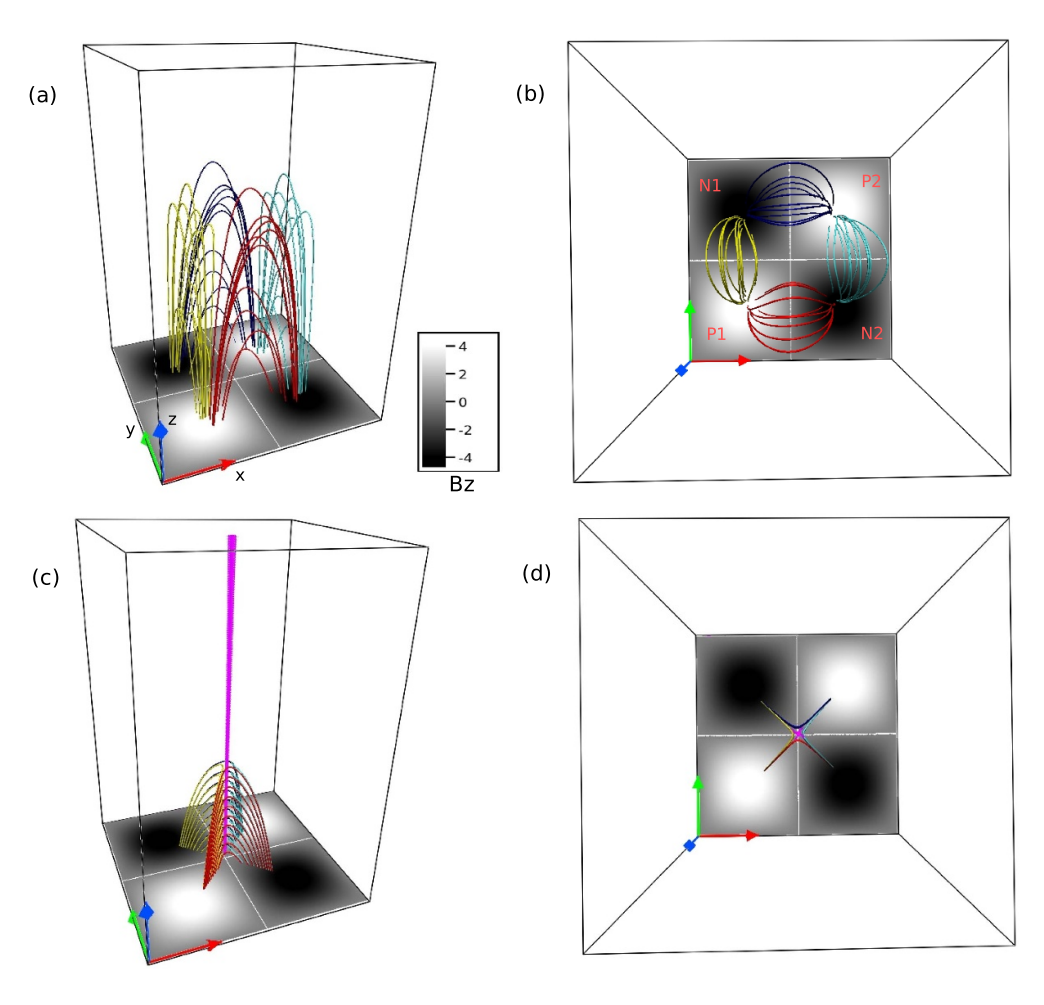


Figure 2. The figure depicts the initial magnetic field overlaid with B_z -contours at the bottom boundary. The corresponding magnetic field lines have a geometry similar to the coronal loops (panel (a)). The quadrupolar magnetic configuration is evident in panel (b) by the presence of two positive polarities (marked by P1 and P2) and two negative polarities (denoted by N1 and N2) separated by PILs (white lines). Panel (c) shows the existence of a neutral line (in pink) at $(x,y) = (\pi,\pi)$ along the z axis inside the domain. The X-type geometry of the field lines near the neutral line (see panel (d)) confirms that the line is made of X-type neutral points.

by white lines in the figure. Noticeably, the opposite polarities satisfy mirror symmetry across the PILs. Because of the mirror symmetry, the initial magnetic field supports an X-type neutral line (made of magnetic neutral points with X-type field line geometry) located at $(x,y) = (\pi,\pi)$ along z (shown in pink in panel (c)). As a result, when seen from the top, the initial field line geometry is quadrupolar (panel (d)). In addition, since the computational domain is periodic along x and y, the initial field also has neutral lines at the domain's boundaries (not shown). The locations of these lines are $(x, y) = (0, 0), (0, \pi), (0, 2\pi),$ $(\pi,0), (2\pi,0), (\pi,2\pi), (2\pi,\pi), \text{ and } (2\pi,2\pi) \text{ along } z \text{ axis. The}$ initial magnetic field with the two positive and negative polarities resembles the observed quadrupolar magnetic configurations at the solar surface [23, 25]. However, in the absence of mirror symmetry and periodicity, the observed configurations exhibit a more complex MFL topology.

3. Governing MHD equations and numerical model

With a focus on exploring the changes in field line topology, here we consider the plasma to be incompressible, thermally inactive, and perfectly conducting [30, 37]. The set of dimensionless MHD equations is then given as:

$$\frac{\partial \mathbf{v}}{\partial t} + (\mathbf{v} \cdot \nabla) \mathbf{v} = -\nabla p + (\nabla \times \mathbf{B}) \times \mathbf{B} + \frac{\tau_a}{\tau_\nu} \nabla^2 \mathbf{v}, \quad (4)$$

$$\nabla \cdot \mathbf{v} = 0, \tag{5}$$

$$\frac{\partial \mathbf{B}}{\partial t} = \nabla \times (\mathbf{v} \times \mathbf{B}),\tag{6}$$

$$\nabla \cdot \mathbf{B} = 0, \tag{7}$$

in usual notations. The magnetic field strength **B** and the plasma velocity **v** are normalized by the average magnetic field strength (B_0) and the Alfvén speed $(v_a \equiv B_0/\sqrt{4\pi\rho_0})$ with ρ_0 representing the constant mass density), respectively. The plasma pressure p, the spatial-scale L, and the temporal scale t are normalized by ρv_a^2 , the size of the system (L_0) , and the Alfvénic transit time $(\tau_a = L_0/v_a)$, respectively. In

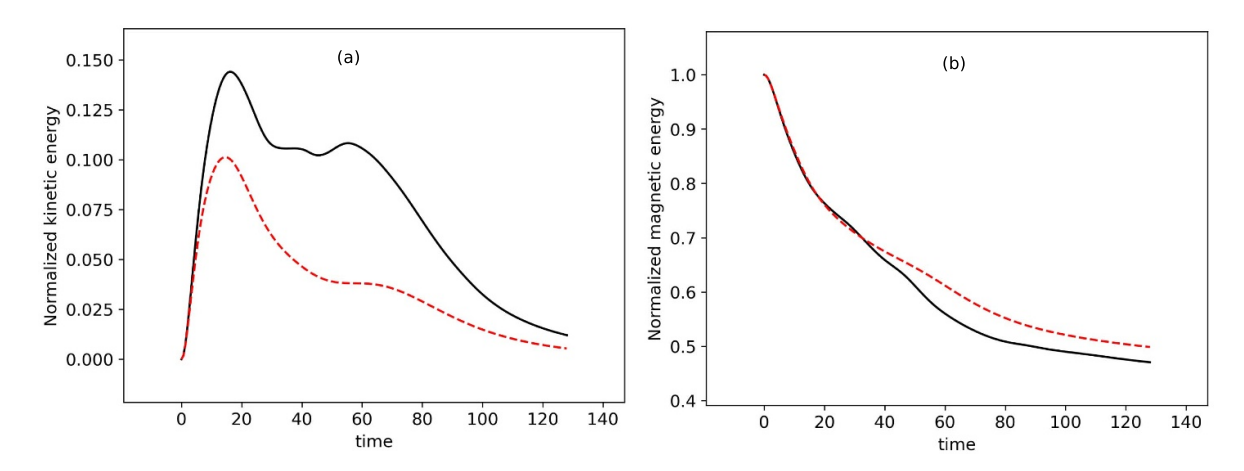


Figure 3. Time evolution of normalized kinetic and magnetic energies for $\nu = 0.005$ (black solid line) and $\nu = 0.01$ (red dashed line). Time has units of seconds. The energies are normalized to the initial total energy. The plots highlight the formation of peaks in kinetic energy. Lower height in the kinetic energy peaks for higher viscosity is in agreement with the general understanding.

equation (4), τ_{ν} represents viscous diffusion time scale ($\tau_{\nu} = L_0^2/\nu$), with ν being the kinematic viscosity.

Notably, the incompressibility (equation (5)) leads to the volume-preserving flow, an assumption routinely used in other works [38, 39]. While compressibility is essential in exploring the thermodynamics of the coronal plasma [40], in this work, our focus is on the changes in the magnetic topology of the initial quadrupolar magnetic configuration. Furthermore, utilizing the discretized incompressibility constraint, the pressure *p* satisfies an elliptic boundary value problem on the discrete integral form of the momentum equation (equation (4)); see [41] and the references therein.

For the numerical solutions of the MHD equations, we use the well-established magnetohydrodynamic numerical model EULAG-MHD [42]. The model is an extension of the hydrodynamic model EULAG predominantly used in atmospheric and climate research [43]. Here we discuss only the essential features of the EULAG-MHD code and refer the readers to [42] and references therein for detailed discussions. The model is based on the spatiotemporally second-order accurate nonoscillatory forward-in-time multidimensional positive definite advection transport algorithm, MPDATA [44]. Importantly, MPDATA has the proven dissipative property which, intermittently and adaptively, regularizes the under-resolved scales by simulating MRs and mimicking the action of explicit subgrid-scale turbulence models [45] in the spirit of implicit large eddy simulations (ILES) [46]. Such ILESs conducted with the model have already been successfully utilized to simulate reconnections to understand their role in the coronal dynamics [16, 17, 47–49]. In this work, the presented computation continues to rely on the effectiveness of ILES in regularizing the commencement of MRs.

4. Simulation results

The simulations are performed over a grid of $128 \times 128 \times 384$, in x, y, and z directions. The magnetic field given by equations (1)–(3) (shown in figure 2) serves as the initial magnetic field for the simulations. The initial velocity is set

to zero (i.e. ${\bf v}=0$). The boundary condition along z is kept open by continuing the ${\bf B}$ to the boundary in order to vanish the net magnetic flux passing through it [17]. Moreover, the boundaries along x and y are taken to be periodic. The simulations are done for two different viscosities $\nu=0.005$ and 0.01. The values of the dimensionless constant τ_a/τ_ν in equation (4) are $\approx 10^{-4}$ and $\approx 10^{-3}$ for the viscosities $\nu=0.005$ and 0.01 respectively, which are larger than its typical coronal value ($\approx 10^{-5}$) [17]. The higher values of τ_a/τ_ν used in the simulations are only expected to speed up the dynamical evolution and reduce the computational cost without affecting the magnetic topology.

For a general understanding of the simulated viscous relaxation, figure 3 shows the time profile of the kinetic (panel (a)) and magnetic energies (panel (b)), normalized to the initial total (magnetic + kinetic) energy. The black solid and red dashed lines correspond to viscosities $\nu = 0.005$ and 0.01, respectively. With an initially vanishing velocity field, the initial Lorentz force triggers the dynamical evolution and generates the plasma flow at the expense of the magnetic energy. The flow is then arrested by the viscous drag, which results in the formation of peaks in kinetic energy plots. Notably, the field lines being frozen into the plasma get deformed by the flow, modifying the initial distribution of the Lorentz force. The peak heights are lower for the simulation with $\nu = 0.01$ in comparison to the simulation with $\nu = 0.005$, which is expected due to the larger magnitude of the viscous drag force for $\nu = 0.01$.

To explore the possibility of flux rope formation, in figure 4, we first describe the evolution of the quadrupolar magnetic field configuration for the computation with viscosity $\nu = 0.005$. The figure further shows the twist parameter, which is calculated by integrating field-aligned current $\mathbf{J} \cdot \mathbf{B}/B^2$ along a field line [50, 51]. Figure 4(b) documents the generation of the twisted MFLs from the initial magnetic loops. These field lines are co-located with the high values of the twist parameter—suggesting the helical nature of the field lines. Hence, the twisted field lines represent MFRs located above the PILs. Initially, there are four separate MFRs,

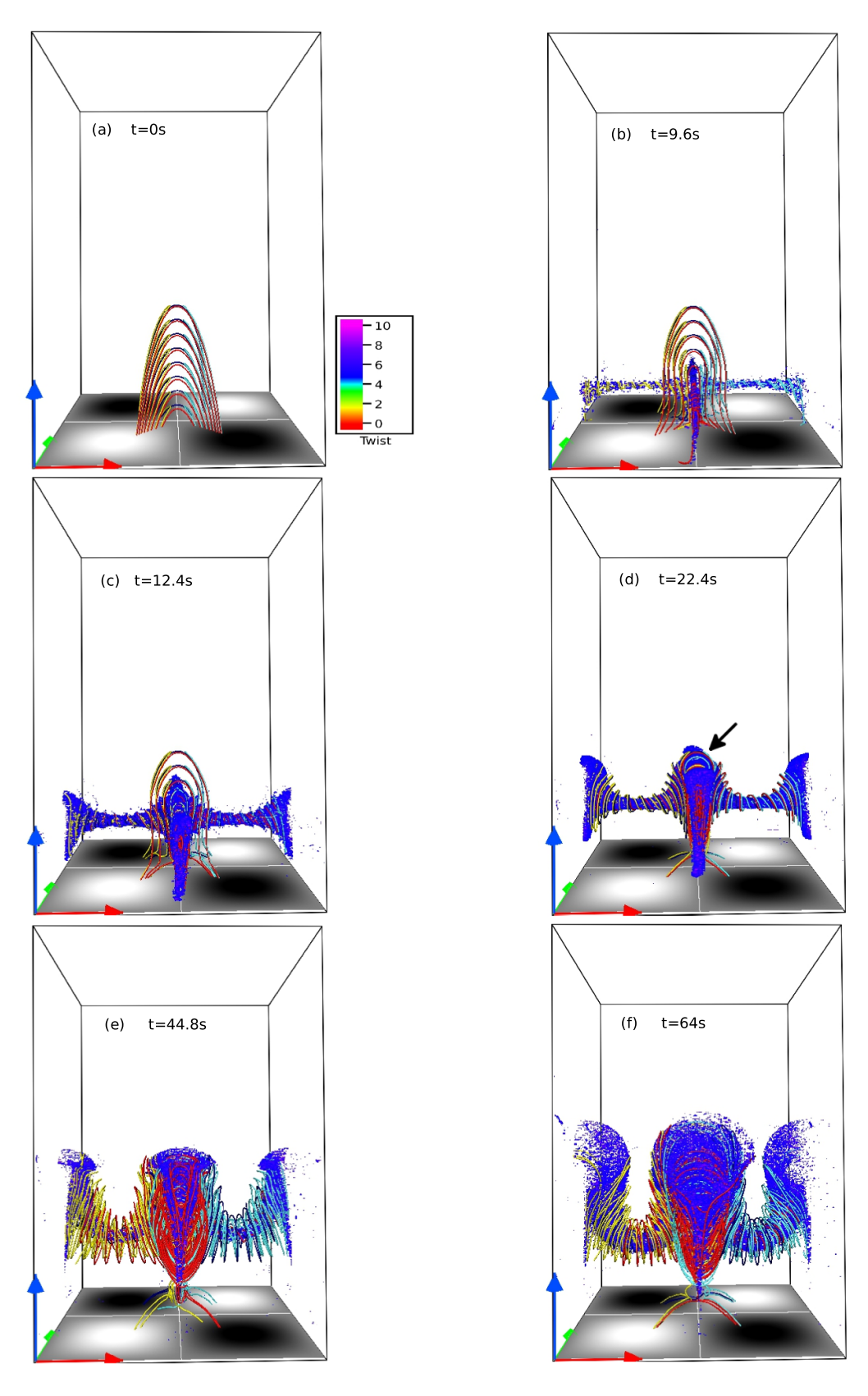


Figure 4. The MHD evolution of the initial quadrupolar magnetic configuration that is overlaid with the twist parameter. Initially, four separate MFRs are generated (panel (b)), which drift toward the X-type neutral lines at $(x,y,z) = (\pi,\pi,z)$, $(0,\pi,z)$, $(\pi,0,z)$, $(\pi,2\pi,z)$, $(2\pi,\pi,z)$ and fuse into complex magnetic structures (panels (c)–(e)). The structure around the X-type neutral line situated in the central part of the domain is marked by a black arrow in panel (d). The flux ropes also show non-uniform rising motion. Also, we have provided a supplementary animation of the figure for the high-cadence dynamics of the ropes.

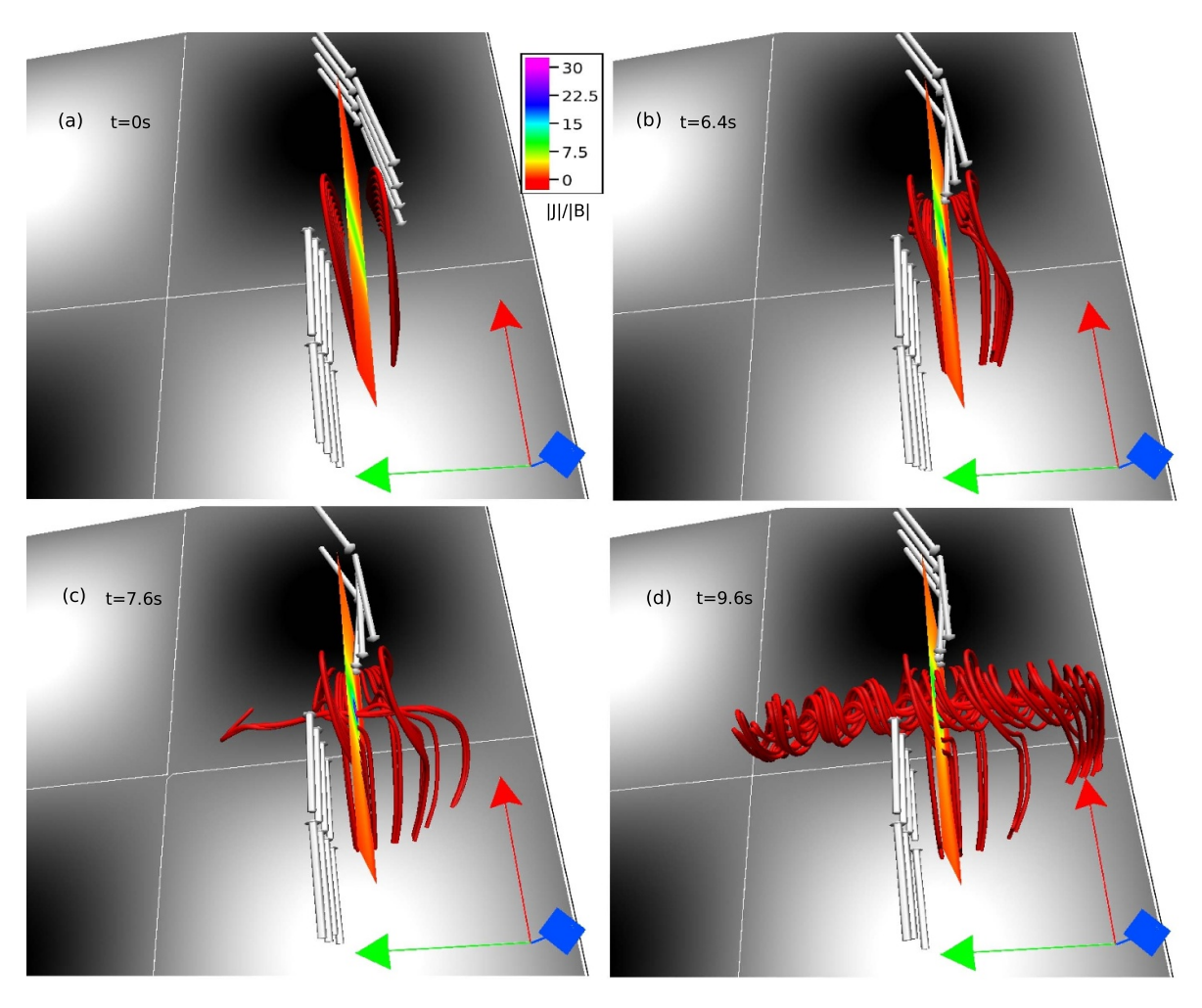


Figure 5. Early phase of the dynamics of the two sets of the bipolar loops situated over the PIL between the P1 and N2 regions (figure 2) overplotted with $|\mathbf{J}|/|\mathbf{B}|$ contours on a *y*-constant plane. The Lorentz force is further shown with grey-colored arrows. Notable are the contortions of the MFLs from the different loops under the favourable Lorentz force, which bring oppositely directed MFLs in proximity, as evident by the higher values of $|\mathbf{J}|/|\mathbf{B}|$ in panel (b)). This evolution leads to repeated reconnections and the formation of an MFR over the PIL (panels (c) and (d)).

situated above the PILs of the different opposite polarities (P1, N1), (P1, N2), (P2, N1), (P2, N2); more clearly shown in figure 5. With time, the magnetic flux of the MFRs increases, accompanied by their rise in the vertical direction (panels (c) and (d) of figure 4). However, the rise of the MFRs is not uniform. Moreover, as the MFRs rise, they appear to interact with the pre-existing X-type neutral lines located at $(x,y,z) = (\pi,\pi,z)$, $(0,\pi,z)$, $(\pi,0,z)$, $(\pi,2\pi,z)$, $(2\pi,\pi,z)$ and, develop complex magnetic structures around them. The structure is more evident around the X-type neutral line that exists inside the computational domain at $(x,y,z) = (\pi,\pi,z)$ as shown in figure 2(c) and marked by a black arrow in figure 4(d). Further, the structures expand and rise with time (panels (e)–(f) of figure 4). A similar evolution is also found for the computation with viscosity $\nu = 0.01$ (not shown).

To closely examine the mechanism of the MFR formation, in figure 5, we focus on the early evolution of two sets of the bipolar magnetic loops located over the PIL corresponding to the regions P1 and N2 (figure 2). The figure is further overlaid with the contours of $|\mathbf{J}|/|\mathbf{B}|$ on a y-constant plane and

the Lorentz force (whose direction is represented by the greycolored arrows). The direction of the Lorentz force is such that the force pushes the two complementary anti-parallel field lines of the different set, located on the opposite sides of the PIL, toward each other (figures 5(a) and (b)). Consequently, the gradient in **B** sharply increases, as evident from a cospatial enhancement in $|\mathbf{J}|/|\mathbf{B}|$. These dynamics lead to the onset of reconnections as the scales become under-resolved (figure 5(c)). The reconnections continue in time and are central to developing an MFR over the PIL. In figure 6, we overplot the two sets with the contours of the logarithm of squashing factor Q on a y-constant plane to support the onset of the reconnections further. The Q-factor is a measure of the gradient in field line mapping of the magnetic field [52] and is calculated using the code of [51]. Notable is the generation of high values of ln Q as the oppositely directed field lines approach each other. The high $\ln Q$ is co-spatial with the high $|\mathbf{J}|/|\mathbf{B}|$ (figure 5)—further supporting the development of the sharp gradient in B and consequent reconnections that lead to the MFR formation. After its formation, the legs of the MFR move

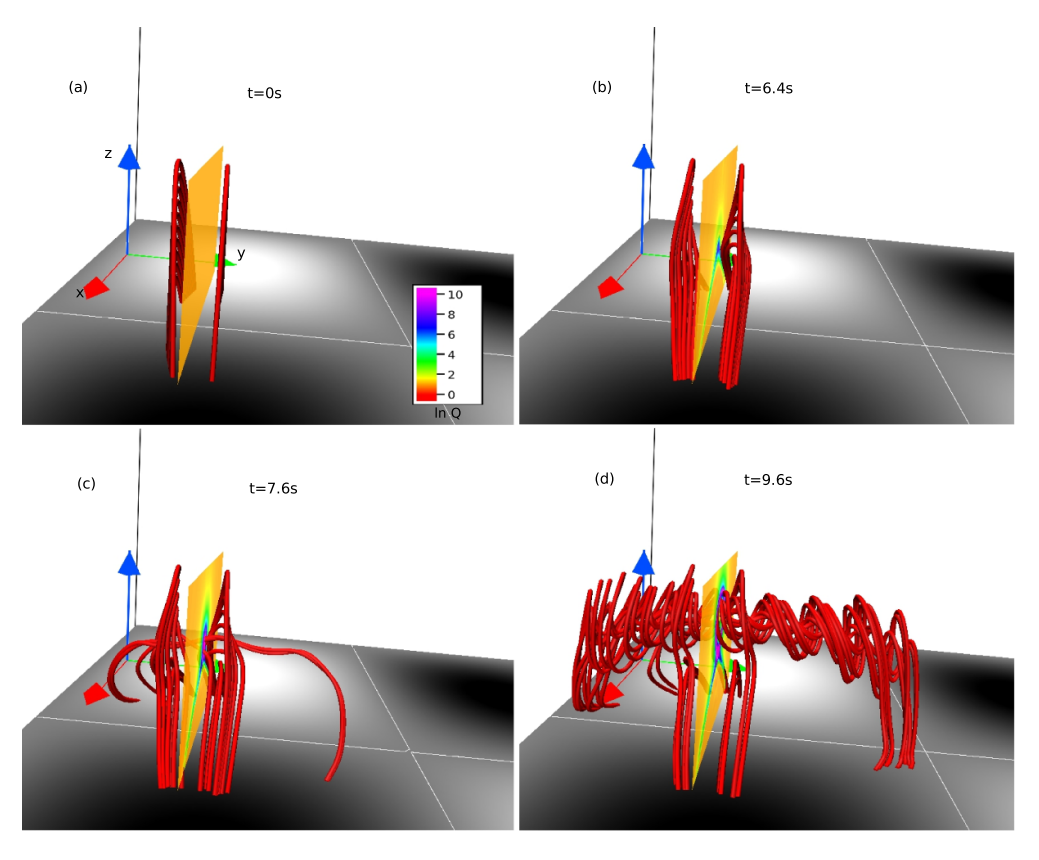


Figure 6. Similar to figure 5, but overplotted with $\ln Q$ contours on a y-constant plane. Higher values of $\ln Q$ in the vicinity of the contorted MFLs further confirm the generation of a high gradient in the magnetic field and consequent reconnections, which are responsible for the MFR formation.

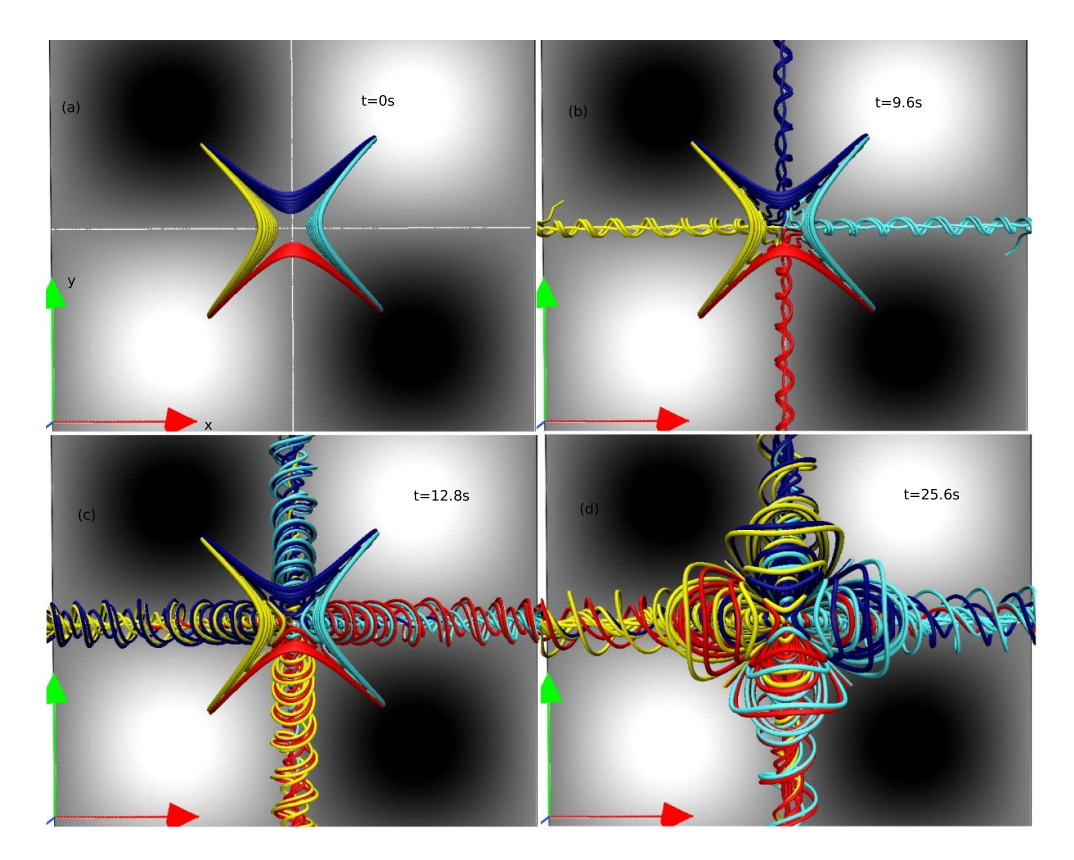
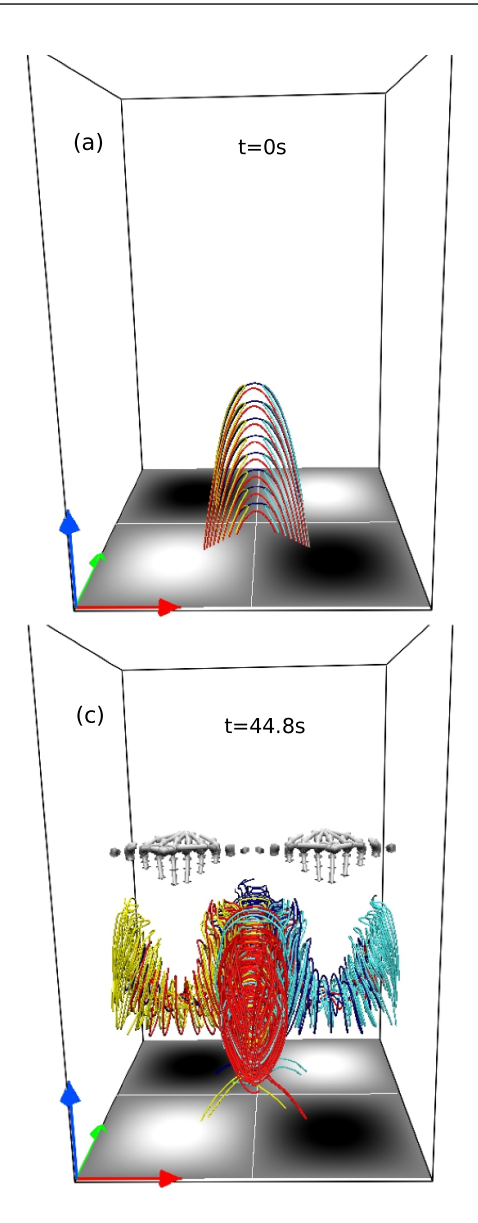


Figure 7. The zoomed-in top view of the MHD evolution of the magnetic field lines near the X-type neutral line inside the computational domain. Reconnections of the flux ropes at the X-type neutral line are evident—leading to the formation of complex magnetic structures.



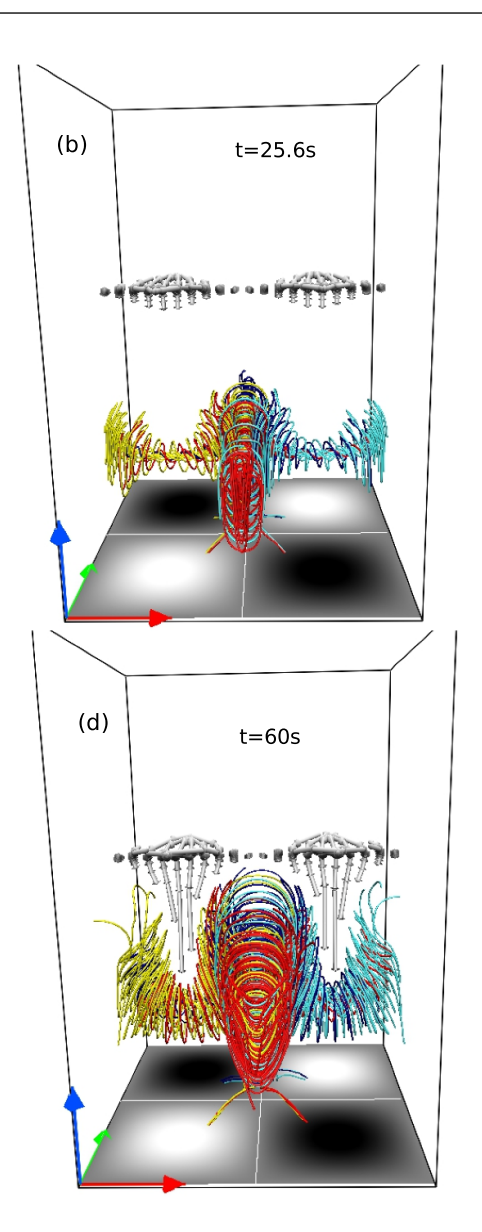


Figure 8. Evolution of the quadrupolar MFLs overlaid with the Lorentz force (grey-colored arrows). The almost negligibly-small Lorentz force over the complex magnetic structures is notable, while the force is mostly vertically downward over the remaining parts of the ropes. Hence, this allows the faster rise and expansion of the structures than the rest. Also, a supplementary animation is provided for a high-cadence evolution.

towards the X-type neutral lines (panels (c) and (d) of figures 5 and 6). A similar process of reconnection also takes place over the other PILs located between (P1, N1), (P2, N1), and (P2, N2)-regions and is responsible for the formation of MFRs over the PILs (not shown).

In figure 7, we plot the top view of the time evolution of the MFLs near the X-type neutral line located inside the central region of the domain at $(x,y,z)=(\pi,\pi,z)$. The figure illustrates that, as the legs of the four MFRs approach the X-type neutral line, they start to reconnect at the neutral line and develop the complex magnetic structure around the neutral line. As these reconnections repeat, more and more magnetic flux is sucked into the central region—shaping the structure and, ultimately, expanding it. Formation of the complex structures through similar dynamical evolution is also observed around the other neutral lines situated at the boundaries of

the domain with the coordinates $(x,y,z) = (0,\pi,z)$, $(\pi,0,z)$, $(\pi,2\pi,z)$, $(2\pi,\pi,z)$ (not shown).

Further, the outflows generated from the repeated reconnections occurring below the flux ropes push them in the vertical direction and lead to the ascent of the flux ropes. Notable is the non-uniform ascent of the flux ropes. The flux ropes show a faster rise and expansion near the neutral lines than away from them (see figure 4). To explore this non-uniform ascent, in figure 8, we plot the evolution of the flux ropes overlaid with the Lorentz force (represented by the grey-colored arrows). The direction and length of the arrows mark the direction and magnitude of the Lorentz force. The figure shows that the Lorentz force is almost negligible around the X-type neutral line (over the complex magnetic structure), while the force is vertically downward away from the neutral line. Moreover, the magnitude of the vertically downward force appears to

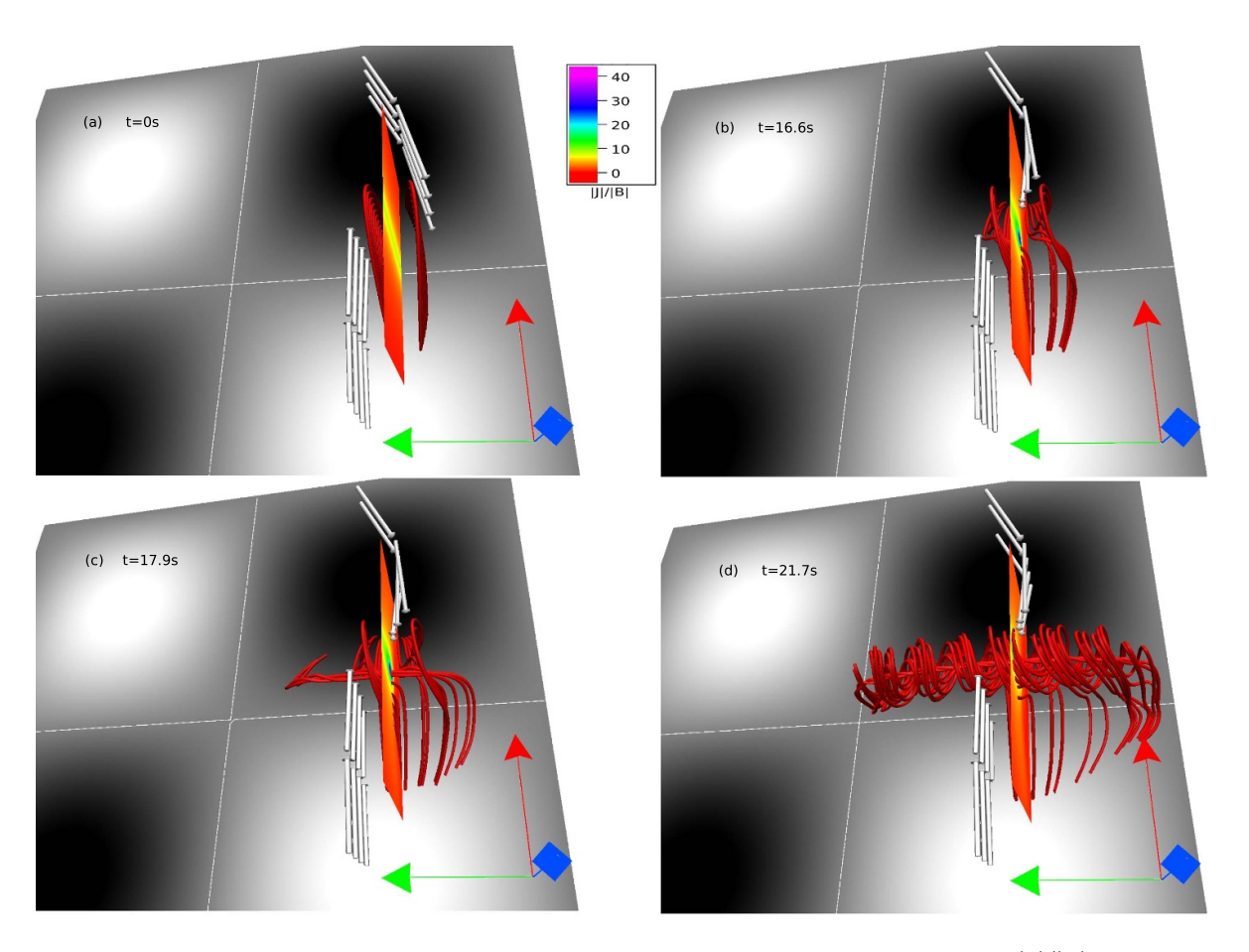


Figure 9. Similar to figure 5, but with the higher resolution of $160 \times 160 \times 480$. Notable is the higher value of $|\mathbf{J}|/|\mathbf{B}|$ in compare to figure 5. The field line evolution is morphologically identical to the ones shown in figure 5.

increase with time. As a result, the overlying Lorentz force does not affect the rise of the flux ropes in the vicinity of the neutral line, while the vertically downward force restricts the rise of the ropes away from the neutral line. This result suggests that the non-uniform rise of the ropes is related to the non-uniform distribution of the overlying Lorentz force.

To show the convergence of the simulation results with increasing resolution, we have also performed an additional higher resolution simulation over a grid of $160 \times 160 \times 480$, in x, y, and z directions with viscosity $\nu = 0.01$. Figure 9 illustrates the time evolution of the two sets of the bipolar magnetic loops in the same sub-domain as shown in figure 5. Moreover, similar to figure 5, figure 9 is also overplotted with the contours of $|\mathbf{J}|/|\mathbf{B}|$ on a y-constant plane and the Lorentz force (whose direction is marked by the grey-colored arrows). For the higher resolution simulation, the maximum value of $|\mathbf{J}|/|\mathbf{B}|$ is increased (see panel (a) of figures 5 and 9) agreeing with the general understanding that the gradient in the magnetic field enhances with an increase in grid resolution. The field line evolution in figure 9 is geometrically identical to the ones depicted in figure 5—confirming the convergence of the results with increasing resolution. Moreover, figure 9 documents a delay in the onset of the reconnection, with an increase in grid resolution. The delay is expected as the under-resolved scales develop later in time with an increased resolution.

5. Summary

The presented MHD simulations explore the MFR formation process in the presence of a quadrupolar magnetic field topology. The initial non-force-free magnetic field is constructed analytically by modifying a three-dimensional linear force-free field having field line geometry similar to the observed coronal loops. The configuration consists of two positive polarity regions, P1 and P2, and two negative polarity regions, N1 and N2. Because of these different polarity regions, the initial field has an X-type neutral line inside the computational domain. In addition, X-type neutral lines also reside at the domain's boundaries due to the periodicity in the lateral directions. Furthermore, the field supports Lorentz force, which naturally generates the simulated dynamics from an initial motionless state. The plasma evolution is idealized to be viscid, incompressible, and thermally homogeneous. Furthermore, the locally adaptive dissipation of the MPDATA scheme mimics the MRs in response to the development of the under-resolved scales.

In the simulations, we first notice the movement of oppositely directed field lines of bipolar loops located above the PILs (separating the different polarity regions) towards each other. This evolution leads to a steep enhancement in the magnetic field gradient and the generation of under-resolved scales.

Consequently, repetitive reconnections initiate and account for the formation of flux ropes over the PILs. In addition, the outflow generated by these reconnections pushes the flux ropes in the upward direction and contributes to their ascent.

With time, the legs of the MFRs move toward the X-type neutral lines and start reconnecting at the line—leading to the generation of complex magnetic structures around the neutral lines. Hence, the simulations demonstrate the topologically complex MFR evolution in the quadrupolar configuration than those found in bipolar magnetic loops [15], which is a key finding of the paper. Furthermore, the rise of the flux ropes is found to be non-uniform. The flux rope near the neutral lines exhibits a faster rise than away from the neutral lines. The non-uniform rise is attributed to the non-uniform generation of the overlying Lorentz force. The Lorentz force is negligible near the neutral lines and enhances with a vertically downward direction as the distance from the neutral lines increases.

Overall, the reported simulations identify spontaneous repeated MRs as the initial driver for the flux rope formation and triggering its ascent in the quadrupolar magnetic configuration. Notably, the ascent of the flux ropes having underlying reconnections is in harmony with contemporary observations at multiple channels (hard x-ray and EUV) that reveal intense localized brightenings below a rising flux rope [53, 54]. More importantly, the pre-existing X-type neutral line and the newly formed flux ropes find morphological similarity to the brightenings observed in EUV images during the flaring events in the quadrupolar magnetic configurations (see [23, 25]). The similarity indicates that the pre-existing X-type neutral points as well as the formation of the flux ropes in the magnetic configurations can play a crucial role in initiating the flaring events. However, the presented simulations, idealized with an analytically constructed initial field and the assumed incompressibility, are only partly conclusive. Therefore, we set a future goal to perform a fully compressible MHD simulation initiated by the extrapolated coronal magnetic field with the observed quadrupolar magnetic configuration, which is expected to provide more realistic coronal dynamics and can be directly compared with solar observations.

Data availability statement

The data that support the findings of this study are available upon reasonable request from the authors.

Acknowledgments

We acknowledge the visualization software VAPOR (www.vapor.ucar.edu) for generating relevant graphics. A P would also like to acknowledge the support of the Research Council of Norway through its Centres of Excellence scheme, Project Number 262622, and Synergy Grant Number 810218 459 (ERC-2018-SyG) of the European Research Council. A P also acknowledges partial support from NSF Award AGS-2020703. S S N acknowledges the NSF-AGS-1954503 and NASA-LWS-80NSSC21K0003 Grants.

ORCID iDs

References

- [1] Priest E 2014 *Magnetohydrodynamics of the Sun* (Cambridge: Cambridge University Press)
- [2] Aschwanden M J 2004 Physics of the Solar Corona. An Introduction (Chichester: Praxis Publishing Ltd)
- [3] Moser A L and Bellan P M 2012 Nature 482 379
- [4] Van Compernolle B and Gekelman W 2012 *Phys. Plasmas* 19 102102
- [5] Elgarhy M A I, Lee M, Kim J Y and Chung K-J 2022 AIP Adv. 12 015110
- [6] Shibata K and Magara T 2011 Living Rev. Sol. Phys. 8 6
- [7] Gibson S E and Fan Y 2006 Astrophys. J. 637 L65–L68
- [8] Fan Y 2009 Living Rev. Sol. Phys. 6 4
- [9] Fan Y 2010 Astrophys. J. **719** 728–36
- [10] Fang F and Fan Y 2015 Astrophys. J. **806** 79
- [11] van Ballegooijen A A and Martens P C H 1989 *Astrophys. J.* 343 971
- [12] Moore R L, Sterling A C, Hudson H S and Lemen J R 2001 Astrophys. J. 552 833–48
- [13] Amari T, Luciani J F, Aly J J, Mikic Z and Linker J 2003 Astrophys. J. 585 1073–86
- [14] Aulanier G, Török T, Démoulin P and DeLuca E E 2010 Astrophys. J. **708** 314–33
- [15] Kumar S, Bhattacharyya R, Joshi B and Smolarkiewicz P K 2016 Astrophys. J. 830 80
- [16] Prasad A, Bhattacharyya R and Kumar S 2017 Astrophys. J. 840 37
- [17] Prasad A, Bhattacharyya R, Hu Q, Kumar S and Nayak S S 2018 Astrophys. J. 860 96
- [18] Prasad A, Dissauer K, Hu Q, Bhattacharyya R, Veronig A M, Kumar S and Joshi B 2020 Astrophys. J. 903 129
- [19] Török T and Kliem B 2005 Astrophys. J. 630 L97-L100
- [20] Kliem B and Török T 2006 Phys. Rev. Lett. 96 255002
- [21] Nishio M, Yaji K, Kosugi T, Nakajima H and Sakurai T 1997 Astrophys. J. 489 976–91
- [22] Sun X, Hoeksema J T, Liu Y, Chen Q and Hayashi K 2012 Astrophys. J. 757 149
- [23] Kawabata Y, Inoue S and Shimizu T 2017 *Astrophys. J.* 842 106
- [24] Chintzoglou G, Vourlidas A, Savcheva A, Tassev S, Tun Beltran S and Stenborg G 2017 Astrophys. J. 843 93
- [25] Mitra P K, Joshi B, Veronig A M and Wiegelmann T 2022 Astrophys. J. 926 143
- [26] Hudson T S and Wheatland M S 1999 Sol. Phys. 186 301–10
- [27] Régnier S 2012 Sol. Phys. 277 131-51
- [28] Lowder C and Yeates A 2017 Astrophys. J. 846 106
- [29] Syntelis P, Lee E J, Fairbairn C W, Archontis V and Hood A W 2019 Astron. Astrophys. 630 A134
- [30] Kumar S, Bhattacharyya R and Smolarkiewicz P K 2014 Phys. Plasmas 21 052904
- [31] Parker E N 1972 Astrophys. J. 174 499
- [32] Parker E N 1994 Spontaneous Current Sheets in Magnetic Fields: with Applications to Stellar x-rays (International Series in Astronomy and Astrophysics vol 1) (New York: Oxford University Press)
- [33] Agarwal S, Bhattacharyya R and Wiegelmann T 2022 Sol. Phys. 297 91

- [34] Bhattacharyya R, Janaki M S, Dasgupta B and Zank G P 2007 Sol. Phys. 240 63–76
- [35] Shaikh D, Dasgupta B, Hu Q and Zank G P 2010 J. Plasma Phys. 76 107–16
- [36] Gary G A 2001 Sol. Phys. 203 71-86
- [37] Kumar S, Bhattacharyya R and Smolarkiewicz P K 2015 Phys. Plasmas 22 082903
- [38] Dahlburg R B, Antiochos S K and Zang T A 1991 Astrophys. J. 383 420
- [39] Aulanier G, Pariat E and Démoulin P 2005 Astron. Atrophys. 444 961–76
- [40] Ruderman M S and Roberts B 2002 Astrophys. J. 577 475–86
- [41] Bhattacharyya R, Low B C and Smolarkiewicz P K 2010 Phys. Plasmas 17 112901
- [42] Smolarkiewicz P K and Charbonneau P 2013 *J. Comput. Phys.* 236 608–23
- [43] Prusa J M, Smolarkiewicz P K and Wyszogrodzki A A 2008 Comput. Fluids 37 1193–207
- [44] Smolarkiewicz P K 2006 Int. J. Numer. Methods Fluids 50 1123–44

- [45] Margolin L G, Rider W J and Grinstein F F 2006 *J. Turbul.* 7 15
- [46] Grinstein F F, Margolin L G and Rider W J 2007 Implicit Large Eddy Simulation: Computing Turbulent Fluid Dynamics (Cambridge: Cambridge University Press)
- [47] Nayak S S, Bhattacharyya R, Prasad A, Hu Q, Kumar S and Joshi B 2019 *Astrophys. J.* **875** 10
- [48] Kumar S, Nayak S S, Prasad A and Bhattacharyya R 2021 Sol. Phys. 296 26
- [49] Kumar S, Prasad A, Sarkar R and Bhattacharyya R 2022 Front. Astron. Space Sci. 9 1039061
- [50] Berger M A and Prior C 2006 J. Phys. A: Math. Gen. 39 8321–48
- [51] Liu R, Kliem B, Titov V S, Chen J, Wang Y, Wang H, Liu C, Xu Y and Wiegelmann T 2016 Astrophys. J. 818 148
- [52] Titov V S, Hornig G and Démoulin P 2002 J. Geophys. Res. 107 1164
- [53] Cheng X, Zhang J, Liu Y and Ding M D 2011 Astrophys. J. Lett. 732 L25
- [54] Kushwaha U, Joshi B, Veronig A M and Moon Y-J 2015 Astrophys. J. 807 101